Calculation of the Vertical Velocity in the Asian Summer Monsoon Anticyclone Region Using the Thermodynamic Method With *in situ* and Satellite Data

Dong Guo[1]*, Peijie Shen[1], Chunhua Shi[1]*, Meirong Wang[1]*, Yu Liu[2], Chenxin Zhang[1] and Wenwen Li[1]

[1] Key Laboratory of Meteorological Disaster, Ministry of Education (KLME)/Joint International Research Laboratory of Climate and Environment Change (ILCEC)/Collaborative Innovation Center on Forecast and Evaluation of Meteorological Disasters, Nanjing University of Information Science and Technology, Nanjing, China, [2] State Key Laboratory of Severe Weather, Key Laboratory of Atmospheric Chemistry of CMA, Chinese Academy of Meteorological Sciences, Beijing, China

Correctly calculating the vertical velocity of the Asian summer monsoon anticyclone (ASMA) region is helpful for accurately knowing the ozone stratosphere–troposphere exchange, so as to explore the variation of ozone in the ASMA region. Therefore, the vertical velocity over the ASMA in June, July, August, and September 2012 and 2016 was calculated using the thermodynamic method, which may avoid the deviations produced by the kinematics method using the mass continuity equation. In order to improve the accuracy, we used high-resolution heating rate datasets obtained via the radiation model in Canadian Atmospheric Global Climate Model called CanAM4.3_RAD based on *in situ* observations and revised satellite data from MLS/AIRS. The vertical velocity calculated by the thermodynamic method (V_T) is then compared with the data from ERA-Interim (V_{ERA-I}). In the daytime, values of V_T were similar to V_{ERA-I} and were dominated by ascending motion, although V_T showed descending motion at the western edge of the ASMA below 100 hPa. The intensity of V_T was slightly smaller than that of V_{ERA-I} at lower levels (200–100 hPa) over the ASMA region and significantly weaker above 100 hPa. The situation was more complex at night. Both V_T and V_{ERA-I} showed the convergence of vertical wind at 150 hPa and the divergence at 80 hPa, but V_T had a smaller standard deviation. V_T showed descending in the western and northern ASMA, but V_{ERA-I} only descended in the west. The descending motion in the west, seen in both V_T and V_{ERA-I}, is produced by the heating difference between the Qinghai–Tibet Plateau and the Iranian Plateau. The difference of the two vertical velocities in the northern ASMA may indicate the different understandings of the local Hadley Circulation and local Brewer-Dobson Circulation.

Keywords: vertical velocity, thermodynamic method, Asian summer monsoon anticyclone, *in situ* observations, reanalysis data

INTRODUCTION

About ~99% of all weather phenomena occur in the troposphere, but the stratosphere, which accounts for ~15% of the total mass of the Earth's atmosphere, has an important role in atmospheric studies (Holton, 1990; Dessler and Sherwood, 2004; Aschmann et al., 2009; Bian, 2009; Randel and Jensen, 2013; Zhang et al., 2016). Ozone is mainly present in the ozone layer, about 20 km above the Earth's surface in the stratosphere (Lv et al., 2009; London and Park, 2011; Newman, 2014). The ozone layer absorbs ultraviolet radiation from the Sun and protects the surface biosphere from damaging radiation. Atmospheric fluctuations in the troposphere are uploaded to the stratosphere (Shepherd, 2002; Xie et al., 2012; He et al., 2020a,b; Yu et al., 2020), leading to the abnormal distribution of ozone in the stratosphere (Chen et al., 2019) and affecting the Earth's climate (Bian et al., 2013; Lu and Ding, 2013; Xie et al., 2016; Li et al., 2017). Some anthropogenic ozone-depleting substances (ODSs), such as chlorofluorocarbons (CFCs) and halons, may also be transported to the stratosphere and influence the stratospheric ozone, while stratospheric ozone may transport to the troposphere and influence the tropospheric ozone (Elliot and Rowland, 1987; Schauffler et al., 1999; Butchart and Scaife, 2001; Newman et al., 2009; Oram et al., 2017; Wang et al., 2019, 2020). Research on stratosphere–troposphere exchange is therefore important in studying stratospheric ozone evolution (Liu et al., 2003; Tian et al., 2008; Bian et al., 2011a, 2020; Guo et al., 2012, 2015, 2017; Xie et al., 2012; Pavlov et al., 2013; Zhang H. et al., 2014; Gerber, 2015; Zhang J. et al., 2018). Previous studies have determined the structural distribution, vertical transport, and dynamics (Antokhin and Belan, 2013) of ozone in the stratosphere via LiDAR measurements (Kuang et al., 2012; Pavlov et al., 2013) the inversion of occultation data (Sofieva et al., 2017) and numerical simulations (Yang et al., 2004; Considine et al., 2008).

The Qinghai–Tibet Plateau, with an altitude of about 4,000 m, has an important role in global stratospheric–tropospheric exchange (Liu, 1998, 2007; Fu et al., 2006; Fan et al., 2008; Bian et al., 2011b, 2020; Tian et al., 2017). More research is required into upward transport over the Qinghai–Tibet Plateau as this is the most representative component of ozone in stratospheric–tropospheric exchange (Vaughan et al., 1994; Holton et al., 1995; Lv et al., 2009). The Asian summer monsoon anticyclone (ASMA) region, a stable high-pressure system over the Qinghai–Tibet Plateau in the summer, is the most important region of stratosphere–troposphere exchange (Zhou et al., 1995a; Cong et al., 2001; Chen et al., 2010; Deng et al., 2015; Fan et al., 2017a,b; Li et al., 2017, 2005; Yu et al., 2017; Shi et al., 2018; Yan et al., 2019) and accounts for almost 75% of this exchange process (Rosenlof, 1995; Stohl et al., 2003; Hu et al., 2009; Tian et al., 2009). Because of its existence, the structure and variation of ozone concentrations in the Qinghai–Tibet Plateau region are significantly different from the global average (Zhou and Luo, 1994; Zhou et al., 1995b; Zou and Gao, 1997; Zheng et al., 1998; Gettelman et al., 2004; Park et al., 2007; Vernier et al., 2009; Tang et al., 2019). Using satellite observations, Randel et al. (2010) confirmed that the ASMA region is an important channel for the mass transport from the troposphere to the stratosphere

in summer. Ploeger et al. (2010) found that the timescales, paths, and diffusion of the mass flux are mainly determined by vertical transport. Bergman et al. (2012) proved that this vertical transport mainly relies on the vertical motion caused by the deviation of large-scale horizontal circulation over the ASMA region. Therefore, accurate calculations of the vertical velocity over the ASMA region are required to accurately estimate the transport of ozone.

The reliable calculation of the vertical velocity is a longstanding issue in numerical weather prediction (Krishnamurti and Bounoua, 1996). The vertical velocity is typically inferred from the mass continuity equation, which has been called the kinematics method by previous researchers (Eluszkiewicz et al., 2000; Mahowald et al., 2002; Schoeberl et al., 2003; Chipperfield, 2006). This method has a more simplified form (Cong et al., 2001; Gettelman et al., 2004; Chen et al., 2010; Zhan and Li, 2012). Sherman (1953) estimated the vertical velocity using the vertical equation and Lord and Jacqueline (1988), Uma and Rao (2009), Ploeger et al. (2010), and de Roode et al. (2012) assessed the impact of the vertical velocity scheme on the modeling of transport. Davis et al. (2007) used Doppler radar to estimate the mean vertical velocity of air.

The magnitude of the horizontal divergence is partially canceled in the ASMA region as a result of the opposite signs of the zonal and meridional divergence of the horizontal and vertical winds (Guo et al., 2012) and the divergence is insensitive to small perturbations in the large-scale horizontal circulation (Rex et al., 2008; Ploeger et al., 2010). Therefore, the deviations in calculating the divergence by the kinematic method will be carried over. The thermodynamic method has been used to avoid deviations from the kinematic method in the upper troposphere and lower stratosphere (UTLS) (Kistler et al., 2001; Rex et al., 2008; Ploeger et al., 2010). This method uses the diabatic heating rate to reflect the vertical motion of the atmosphere across the isentropic (θ) surface, and the vertical velocity is determined in a θ coordinate system (Rosenlof, 1995; Eluszkiewicz et al., 1996; Randel et al., 2002; Fueglistaler et al., 2005; Rex et al., 2008). Bergman et al. (2013) showed that numerical solutions are affected by the accuracy and resolution of the heating rates in the thermodynamic method. Some researchers have used satellite data and assimilation datasets to calculate heating rates (Rosenlof, 1995; Eluszkiewicz et al., 1996; Randel et al., 2002) and the results were clearly different (Liu et al., 2003; Yang et al., 2004).

Although some studies have applied the thermodynamic method, there is a lack of such research in the ASMA region. We used the revised satellite detection data from the microwave limb sounder (MLS) and the atmospheric infrared sounder (AIRS) for 2012 and 2016 reported by Shi et al. (2017) and the radiation model in Canadian Atmospheric Global Climate Model called CanAM4.3_RAD (**Appendix A**) to calculate the heating rate. We then applied the thermodynamic equation (Zhou et al., 2014) in isentropic coordinates to introduce a method to calculate the vertical velocity over the ASMA region.

Section "Materials and Methods" of this paper presents the data and methodology. Section "Results" compares the thermodynamic vertical velocity with the reanalysis data in different ways. We discuss the possible reasons for the deviations

and the potential factors influencing the results in section "Discussion and Conclusions."

MATERIALS AND METHODS

Data

ERA-Interim Reanalysis Data
The ERA-Interim (ERA-I) reanalysis dataset has a higher credibility in the Qinghai–Tibet Plateau region than other reanalysis datasets, especially in the UTLS region, and realizes a more accurate description of the interannual variability (Monge-Sanz et al., 2007; Hu et al., 2009; Guo et al., 2017; Huang et al., 2018; Shi et al., 2018). The vertical velocity in the ERA-I dataset has previously been used as the kinematic vertical velocity in this region. We downloaded the ERA-I data directly from the European Centre for Medium-Range Weather Forecasts' website[1], including the horizontal wind (u, v), vertical velocity (ω), and temperature (T) fields. The u, v, T, and p were used to determine the vertical velocity by thermodynamic method, and the ω was compared with the vertical velocity we calculated. The vertical resolution in the isobaric surfaces is 13 layers from 300 to 10 hPa. The horizontal grid resolution is $0.75° \times 0.75°$ and the temporal resolution is 12 h. We used the dataset for the time period June, July, August, and September (JJAS) in 2012 and 2016.

Heating Rate Data
We substituted the heating rate with only the radiative heating rate data and ignored the sensible heat and latent heat. This is because the water vapor phase transition over the ASMA region is not significant as a result of the small amount of water vapor present and the low temperatures. The exchange of sensible heat is weak due to the small vertical temperature lapse rate and convection in the UTLS region. We used the CanAM4.3_RAD developed by Salzen et al. (2013) to calculate the radiative heating rate. This model can provide a high-accuracy simulation of the cloud radiation effect and the Earth's radiation system (Zhang et al., 2013). The concentration of ozone, the temperature, and the water vapor content were required to drive the model and these data were obtained from the *in situ* observational profile of Ali station and the revised satellite dataset from MLS/AIRS.

The Ali dataset was obtained using a balloon-borne electrochemical concentration cell sonde at the Indus River (32.5°N, 80°E) in the central region of the ASMA. The electrochemical concentration cell measured the profiles with an accuracy within 10% in the troposphere and 5% in the stratosphere (Shi et al., 2017). The sounding balloons were launched at midnight from June to September 2016 to an altitude of 30 km. A total of 17 valid ozone profiles were obtained. In order to reduce the deviation taken by the time, human operation, and weather process, the JJAS average of Ali data was used to represent the summer mean.

The revised satellite dataset from the MLS/AIRS was corrected using the Ali dataset based on the MLS Level 2 Version 4

and the AIRS Version 6 Level 2 (L2) Support by different methods in JJAS 2012 and 2016. The original AIRS data had 55 layers from 515 to 10 hPa, and the original MLS data had 33 layers in total from upper troposphere to 0.1 hPa in the vertical direction (Yan et al., 2015; Gamelin and Carvalho, 2017; Herman et al., 2017; Shi et al., 2017). According to the spatial and temporal characteristics of the two data themselves, MLS was observed only in the longitudinal direction, along the horizontal plane of the flight path, while AIRS was observed in both the latitudinal and longitudinal directions, so we processed the MLS/AIRS into different analytical data. In the center of ASMA (about 25°N–42°N, 40°E–100°E), MLS and AIRS were revised by subtracting the summer mean deviation profile of Ali, and in the other area of ASMA, data were corrected by subtracting the half of the summer mean deviation profile of Ali (Shi et al., 2017). Their horizontal resolutions were $1.9° \times 2.5°$ and $1° \times 1°$, respectively. In this way, we obtained the average heating rate at station Ali in JJAS 2016, the mean semi-monthly MLS heating rate, and the daily AIRS heating rate in JJAS 2012 and 2016.

Data Processing
The heating rate and ERA-I reanalysis data were interpolated in the horizontal and vertical directions to obtain the same temporal and spatial resolution before carrying out our calculations. We used typical linear interpolation for u, v, T, ω in the ERA-Interim dataset in the new horizontal grids of $1.9° \times 2.5°$ and $1° \times 1°$, which are consistent with the MLS and AIRS heating rate data. We then interpolated the ERA-Interim data and the heating rate data into the same isentropic layers in the vertical direction. The layers were selected based on a combination of the vertical resolution between the two datasets. In this way, the resolution advantage of each dataset was preserved. The area was limited to (23°N–39°N, 70°E–107°E).

Methods

Calculation of Vertical Velocity
Previous studies (Eluszkiewicz et al., 2000; Mahowald et al., 2002; Schoeberl et al., 2003; Chipperfield, 2006) have shown that the vertical velocity can be determined using the kinematics equation in isobaric coordinates:

$$\omega = \int_{p1}^{p0} \left(\frac{\partial u}{\partial x} + \frac{\partial v}{\partial y} \right) dp \qquad (1)$$

which indicates that ω mainly depends on changes in the divergence term $\frac{\partial u}{\partial x} + \frac{\partial v}{\partial y}$. However, the term $\frac{\partial u}{\partial x} + \frac{\partial v}{\partial y}$ is insensitive to small perturbations in u and v and deviations from the observational data are common. We therefore applied the isentropic (θ) coordinate system:

$$\omega = \left(\frac{dp}{dt} \right)_{\theta} \qquad (2)$$

$$\omega = \left(\frac{dp}{dt}\right)_\theta = \left(\frac{\partial p}{\partial t}\right)_\theta + (\vec{V} \cdot \nabla p)_\theta \tag{3}$$

$$\omega = \left(\frac{\partial p}{\partial t}\right)_\theta + \left(u\frac{\partial p}{\partial x} + v\frac{\partial p}{\partial y} + \omega_\theta \frac{\partial p}{\partial \theta}\right)_\theta \tag{4}$$

Eq. 2 gives a method to determine the vertical wind by directly solving the pressure change rate in the isentropic coordinate system. This is then expanded in θ-coordinates in Eqs 3 and 4.

ω_θ is the vertical wind in θ-coordinates:

$$\omega_\theta = \frac{d\theta}{dt} \tag{5}$$

The general form of the thermodynamic energy equation gives:

$$c_P \frac{dT}{dt} + p\frac{d\alpha}{dt} = \dot{Q} \tag{6}$$

where $\dot{Q}$ (J s^{-1}) is the diabatic heating rate, which means the change of adiabatic heating over time, $c_P = 1{,}000$ J/K·kg, is the specific heat at constant pressure, T (K) is the temperature, and p (Pa) is the atmosphere pressure.

Logarithmic differentiation of the potential temperature equation $\theta = T\left(\frac{P_0}{P}\right)^{R/C_P}$ gives

$$c_P d\ln\theta = c_P d\ln T - R d\ln p \tag{7}$$

where R is the gas constant.

Combine Eq. 7 with Eq. 6 and let $s = c_P \ln\theta$, so that the thermodynamic equation can be written as

$$\frac{ds}{dt} = \frac{\dot{Q}}{T} \tag{8}$$

Transforming this with θ gives

$$\frac{d\theta}{dt} = \frac{\dot{q}}{T} \tag{9}$$

where $\dot{q} = \frac{d\dot{Q}}{dt} = \frac{\theta}{C_P}\dot{Q}$.

Substituting Eq. 9 into Eq. 4, the diagnostic equation for the vertical velocity in isentropic coordinate system is obtained:

$$\omega = \left(\frac{\partial p}{\partial t}\right)_\theta + \left(u\frac{\partial P}{\partial x} + v\frac{\partial P}{\partial y}\right)_\theta + \frac{\partial P}{\partial \theta}\frac{\theta}{T \cdot C_P}\dot{Q} \tag{10}$$

The first term on the right-hand side is the local pressure tendency term, which represents the vertical velocity caused by the isentropic surface moving up and down locally. The second is the airflow advection term along the isentropic surface, which can be used to judge the direction of vertical velocity when the air flows from high to low pressure, producing an ascending motion and vice versa. The last diabatic term indicates that because $\frac{\partial P}{\partial \theta} < 0$, there is ascending motion when there is diabatic heating ($\dot{Q} > 0$) and descending motion when there is diabatic cooling ($\dot{Q} < 0$) (Zhou et al., 2014).

Statistical Analysis

We introduced some statistical variables for quantitative analysis (Rodgers, 1990; Von Clarmann, 2006; Shi et al., 2017):

$$\sigma = \sqrt{\frac{\sum_{i=1}^{n}\left(V_i - \bar{V}\right)^2}{n}} \tag{11}$$

$$b = \frac{\sum_{i=1}^{n}[V_{AIRS}(i) - V_{ERA-I}(i)]}{n} \tag{12}$$

$$se = \sqrt{\frac{\sum_{i=1}^{n}[(V_{AIRS}(i) - V_{ERA-I}(i)) - b]^2}{n(n-1)}} \tag{13}$$
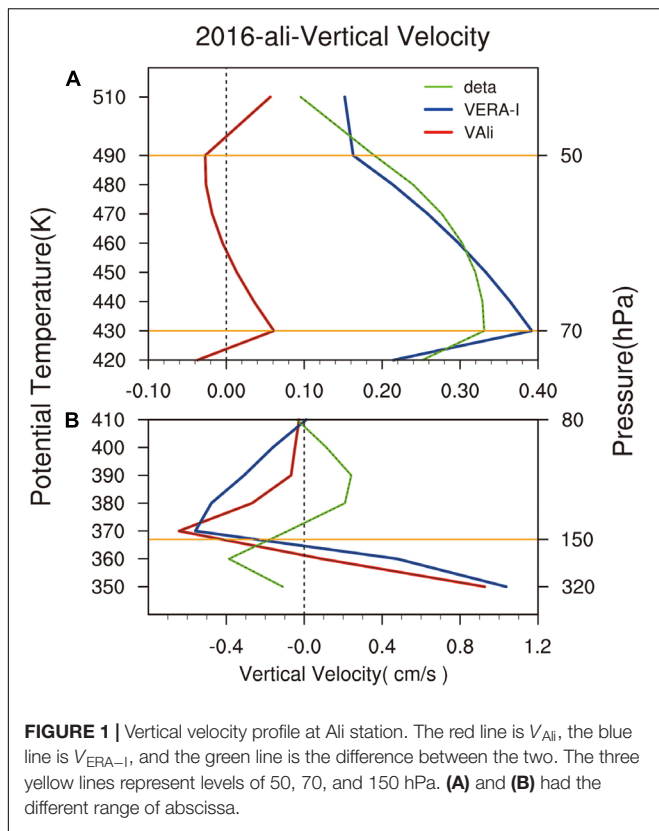
Eq. 11 is the standard deviation (σ) of a variable where V_i is one of the vertical velocity values, the subscript i indicates the different times, and $\bar{V}$ is the mean value. This variable can illustrate the degree of discretization of each vertical velocity. The mean bias (b) in Eq. 12 was applied to describe the degree of deviation between the vertical velocity of the AIRS and ERA-I data. The standard error (se) is used in Eq. 13 to reduce the inaccuracy caused by abnormal or accidental conditions in Eq. 12. It is stipulated that when the interval (b - se, b + se) does not contain the value 0, then the difference between the two datasets described by b will be accepted and the result is considered to be statistically significant.

RESULTS

Substituting three different heating rates into Eq. 10, we calculated the average vertical velocity profiles for Ali station in JJAS (V_{Ali}), the daily vertical velocity data of the AIRS (V_{AIRS}), and the monthly average vertical velocity of the MLS (V_{MLS}). We then compared these results with the vertical velocity in the ERA-Interim (V_{ERA-I}) dataset, which had been interpolated at the same spatiotemporal resolution. We used V_{Ali}, V_{AIRS}, and V_{ERA-I} to analyze the results for Ali station. We compared V_{MLS} with V_{ERA-I} for the ASMA region distribution analysis.

Results for Ali Station

Figure 1 shows the profiles of the nighttime vertical velocity at Ali station. It can be seen that V_{Ali} and V_{ERA-I} had a similar tendency, with a decreasing rate with height below 150 hPa, between 70 and 50 hPa, and an increasing rate with height in the other layers. In terms of the absolute values, the values in V_{Ali} and V_{ERA-I} approach each other below 80 hPa, but are different above 80 hPa. To make the difference clearer, we reduced the range of abscissa in (-0.1 to 0.4) in **Figure 1A**. V_{ERA} shows weaker ascending motion in the range of 70-50 hPa than that below 80 hPa, while V_{Ali} is mainly concentrated near the zero line, indicating insignificant vertical movement in the upper levels. They both indicate the vertical motions in the lower stratosphere (70-50 hPa) is weaker. For two vertical velocities, the wind reversed from ascending to descending around 200 hPa and the intensity of descending motion decreased gradually with increasing height. The vertical velocity reached zero near 80 hPa and the wind direction reversed again to a dominant

FIGURE 1 | Vertical velocity profile at Ali station. The red line is V_{Ali}, the blue line is V_{ERA-I}, and the green line is the difference between the two. The three yellow lines represent levels of 50, 70, and 150 hPa. **(A)** and **(B)** had the different range of abscissa.

ascending movement. The characteristics of low convergence and high divergence over the Qinghai–Tibet Plateau are described simultaneously by these two vertical velocities.

To avoid the influence of a single station, we compared V_{AIRS} with V_{ERA-I} in different layers (**Figure 2**). We chose the regional average over (32.5±2°N, 80.5±2°E) around Ali station to represent the single-point data. **Figure 2** clearly shows that there are significant differences between day and night.

In the daytime, V_{ERA-I} (blue) describes a more pronounced upward movement in the region around Ali station that decreases with height. By contrast, V_{AIRS} only shows a clear ascending motion in the lower layers (200 and 150 hPa) and the values are much lower than V_{ERA-I}. V_{AIRS} approaches zero at 70 hPa.

At night, V_{ERA-I} shows an alternation from ascending to descending motion at 200 hPa and is dominated by descending motion in the range 150–100 hPa. V_{ERA-I} shows a remarkable upward motion in the higher layers around 70 hPa most of the time. V_{AIRS} shows the same variation as V_{ERA-I}, but with smaller values. This is because the radiation heating rate of the atmosphere in the UTLS in the daytime is mainly caused by shortwave solar radiation, which has a strong positive heating effect, leading to upward motion. Most of the heating at night is caused by longwave radiation from the ground, so the heating rate is negative, representing descending motion. The nighttime characteristic represented by V_{AIRS} is consistent with the results of V_{Ali}.

We examined the mean and standard deviation of V_{AIRS} and V_{ERA-I} in JJAS to conduct a more intuitive quantitative

analysis and comparison (**Figure 3**). For the vertical velocity in 2012, V_{AIRS} and V_{ERA-I} are mostly positive in all the layers in the daytime (**Figure 3A**) and V_{AIRS} shows a much weaker updraft than V_{ERA-I}. V_{AIRS} reverses from positive to negative between 150 and 100 hPa, leading to wind convergence with a lower standard deviation; but this is not seen for V_{ERA-I}. The consistency of the distribution of V_{AIRS} and V_{ERA-I} increases during the night-time (**Figure 3C**), especially in the upper stratosphere. The reversal of winds appears near 150 and 80 hPa, consistent with V_{Ali} (**Figure 1**). The standard deviations also show that the dispersion of both V_{AIRS} and V_{ERA-I} gradually decreases with height in the daytime.
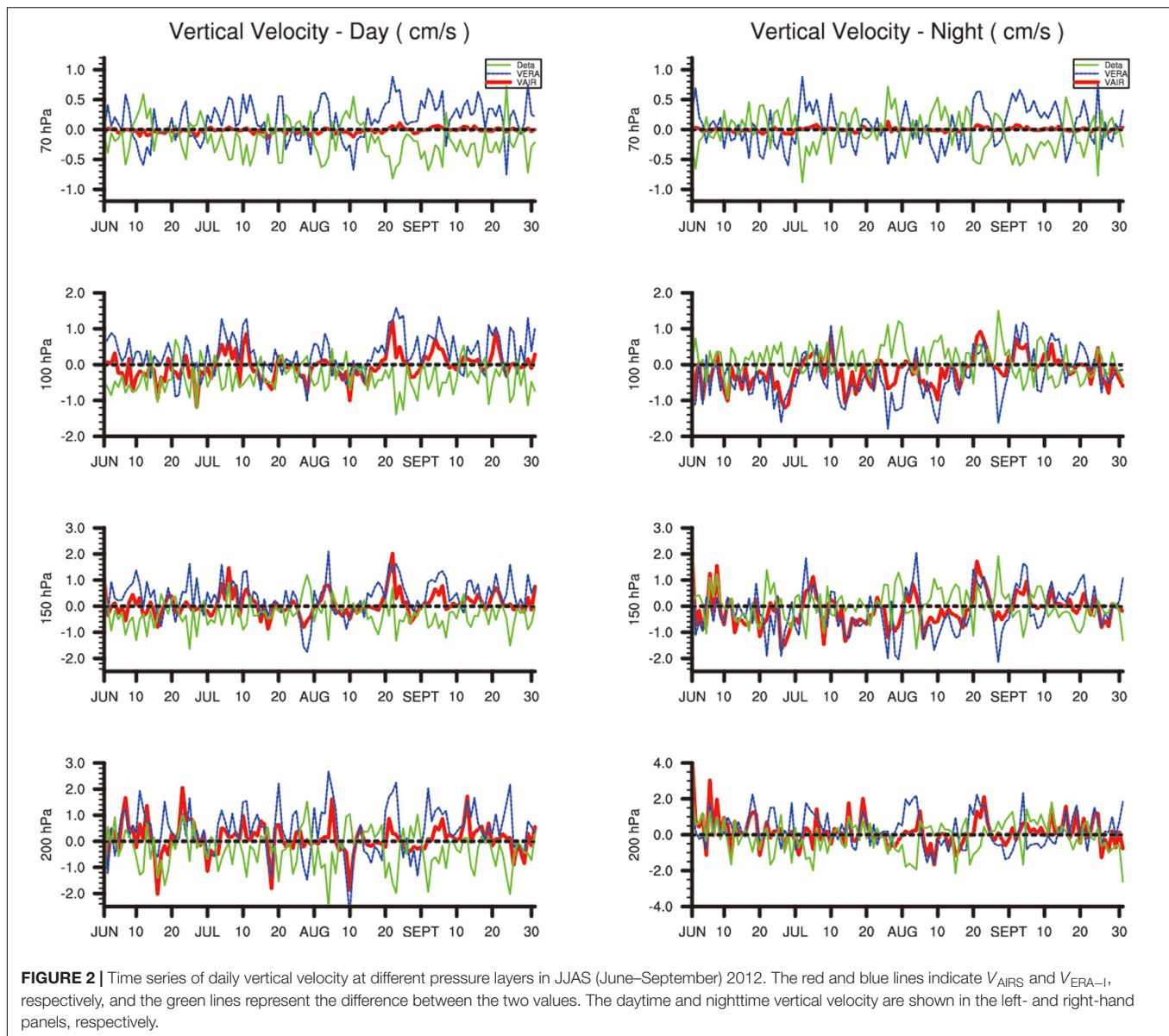
The overall distribution of the mean and standard deviation in 2016 were similar to those in 2012, but the differences between two vertical velocities were more significant than in 2012, especially in the lower stratosphere. The results in 2016 had a greater deviation, especially for V_{AIRS} at night.

We substituted V_{AIRS} and V_{ERA-I} into Eq. 13 and obtained the range (b - se, b + se) to investigate the mean bias and standard error of the vertical velocity (**Figure 4**). According to the daytime results for 2012 (**Figure 4A**) and 2016 (**Figure 4B**), the mean bias is concentrated near zero below 250 hPa, but is almost positive above 250 hPa. This shows that V_{ERA-I} differs slightly from V_{AIRS} in the lower layers, but that the difference is more pronounced at higher levels in the daytime. Above 250 hPa, the range (b - se, b + se) with the error bars does not contain 0. These results show that, in the daytime, the deviations all have more statistical significance above 250 hPa. In other words, V_{ERA-I} is generally higher than V_{AIRS} above 250 hPa.

The results for nighttime are different. In 2012, the mean bias was positive at all layers, which means that V_{AIRS} was smaller than V_{ERA-I}. But combined with the values of error bars, the results were statistically significant above 180 hPa, but insignificant at lower levels. Therefore V_{ERA-I} is larger than V_{AIRS} in the lower stratosphere and the deviation between them in the upper troposphere has more uncertainty. The situation was the opposite in 2016 and was statistically significant at lower levels (250–110 hPa), but not at higher levels.

Regional Comparison Analysis

Using (32.5°N, 80.5°E) as the center point, V_{MLS} was expanded along 32.5°N and 80.5°E to obtain the longitudinal and latitudinal vertical profiles. **Figure 5** shows the characteristics of V_{MLS} and V_{ERA-I} during the daytime in 2012. The latitudinal profiles in **Figures 5A,B** show that both V_{MLS} and V_{ERA-I} have clear ascending motion in most areas of the ASMA and convergence at 80 hPa near 91.25°E (the center of the Qinghai–Tibet Plateau). But V_{MLS} shows descending motion in the west of 91.25°E and below 100 hPa, which is not shown in V_{ERA-I}. In terms of the deviation in **Figure 5C**, V_{MLS} has a weaker latitudinal ascending motion than V_{ERA-I}, especially above 100 hPa, where the differences pass the significance test. According to the longitudinal section in **Figures 5D,E**, upward motion appears simultaneously in most areas of V_{ERA-I} and V_{MLS}. Below 150 hPa, the ascending motion for V_{MLS} (**Figure 5D**) is as strong as V_{ERA-I} (**Figure 5E**), but above 150 hPa, V_{MLS} is clearly weaker than V_{ERA-I}. These differences also have passed the significance

FIGURE 2 | Time series of daily vertical velocity at different pressure layers in JJAS (June–September) 2012. The red and blue lines indicate V_{AIRS} and V_{ERA-I}, respectively, and the green lines represent the difference between the two values. The daytime and nighttime vertical velocity are shown in the left- and right-hand panels, respectively.

test (**Figure 5F**). In contrast, V_{MLS} is negative north of 34.4°N and near 100 hPa, although the intensity is not as strong as for the ascending motion.

The nighttime conditions (**Figure 6**) are different from the daytime conditions (**Figure 5**). In the latitudinal profiles (**Figures 6A,B**), V_{MLS} shows strong descending motion below 150 hPa, whereas V_{ERA-I} shows significant ascending. Above 150 hPa, V_{MLS} is negative west of 91.25°E and positive to the east. Compared with the daytime, the area in which V_{MLS} is descending has expanded to lower and higher layers in the vertical direction. For V_{ERA-I}, descending motion is seen to the west of 91.25°E with a center of intensity near 100 hPa, but the vertical depth of the descending air is less than for V_{MLS}. The latitudinal profiles for V_{MLS} at nighttime and daytime both show descending motion in the west over the ASMA region. That probably indicates there is a difference in the descending branch

of the Hadley Circulation in this region between V_{MLS} and V_{ERA-I}. The Hadley Circulation originally leads to a descending motion, but the stronger heating of the Qinghai–Tibet Plateau in the east and the weaker heating of the Iranian Plateau in the west (Zhang F. et al., 2017) finally introduced a more clearly upward motion over the Qinghai–Tibet Plateau. Thus, the atmosphere in the west descends while the atmosphere in the east ascends. V_{MLS} is more consistent with this explanation both day and night. Meanwhile, V_{MLS} and V_{ERA-I} both clearly show ascending movement in the east of the ASMA region. In the east of 99.25°E, between 100 and 70 hPa, V_{MLS} ascends significantly slowly than V_{ERA-I}, as illustrated in the test of deviation (**Figure 6C**).

The longitudinal sections in **Figures 6D,E** show V_{ERA-I} ascending, but V_{MLS} descending in the northern part of the ASMA and in the lower layers below 150 hPa. With the local Hadley Circulation and the local Brewer-Dobson Circulation
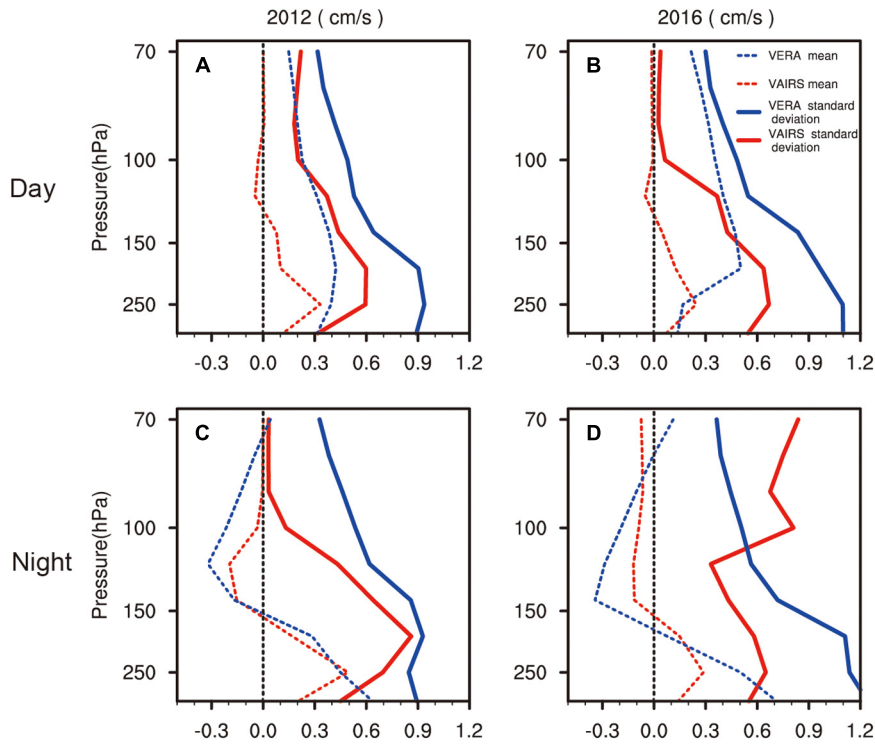
FIGURE 3 | Mean (dashed lines) and standard deviation (solid lines) of V_{AIRS} and V_{ERA-I} in JJAS (units: cm s^{-1}) in 2012 **(A,C)** and 2016 **(B,D)**. The blue lines are V_{ERA-I} and the red are V_{AIRS}. The upper panels are daytime and the bottom panels nighttime.
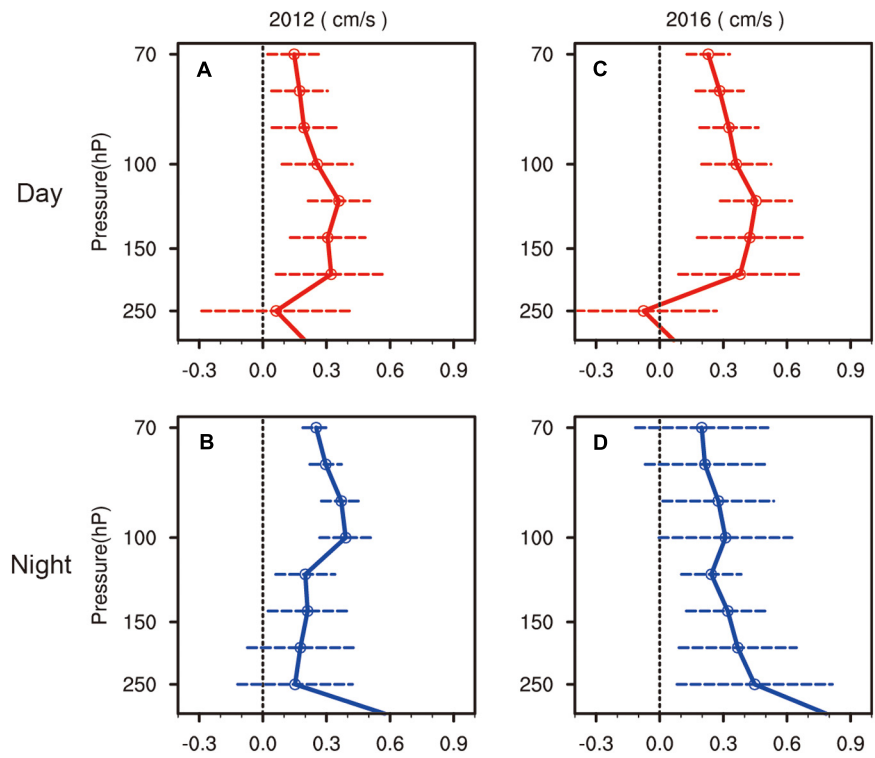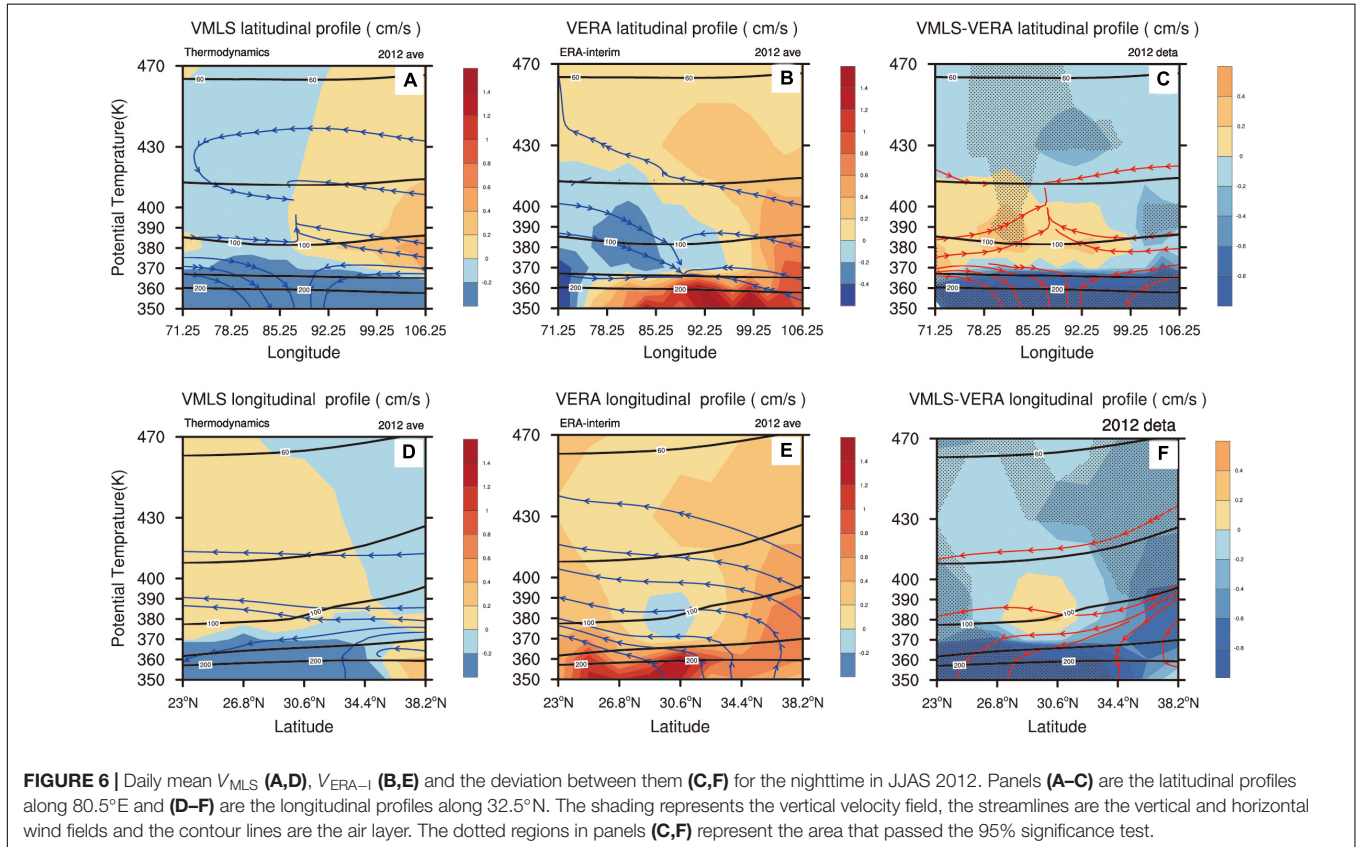

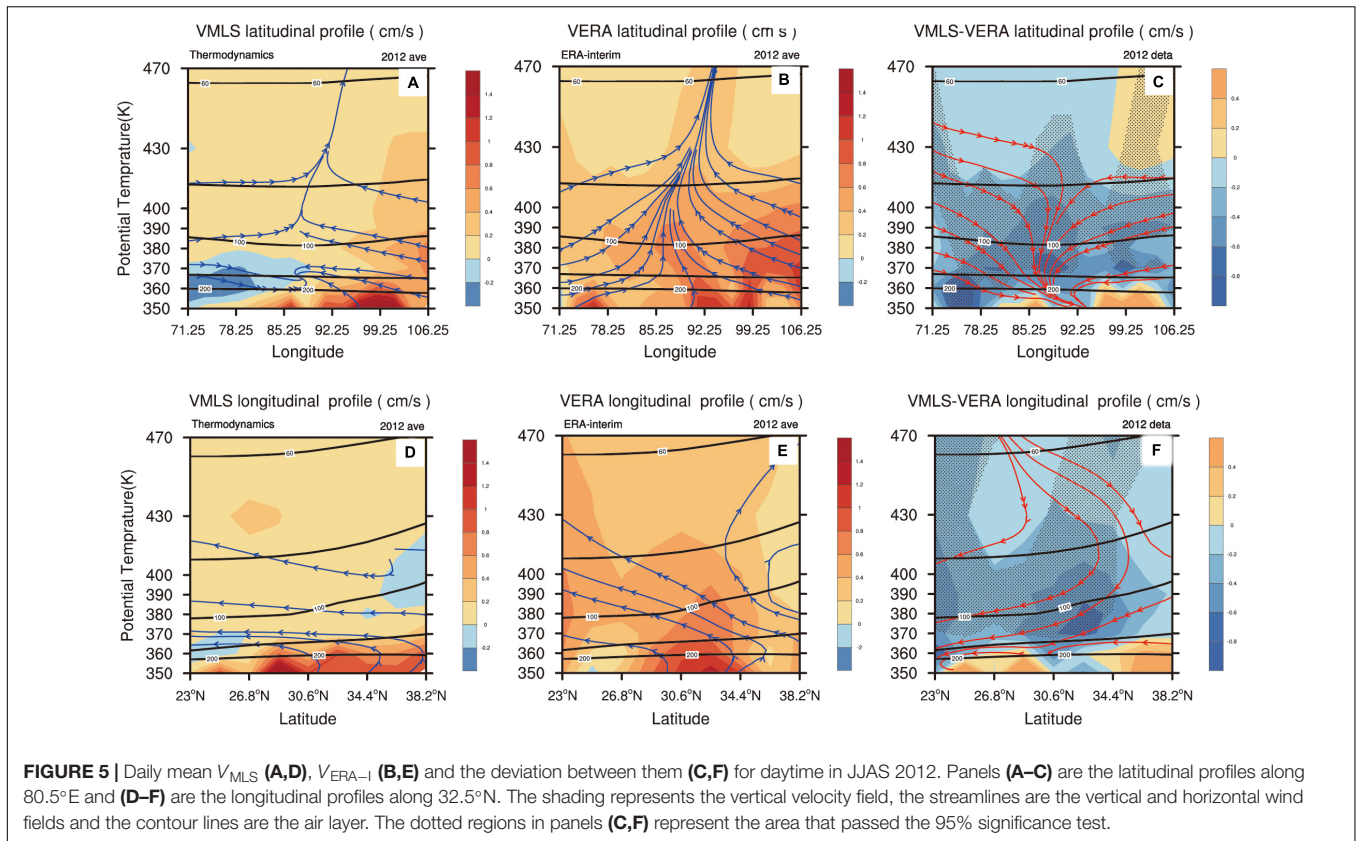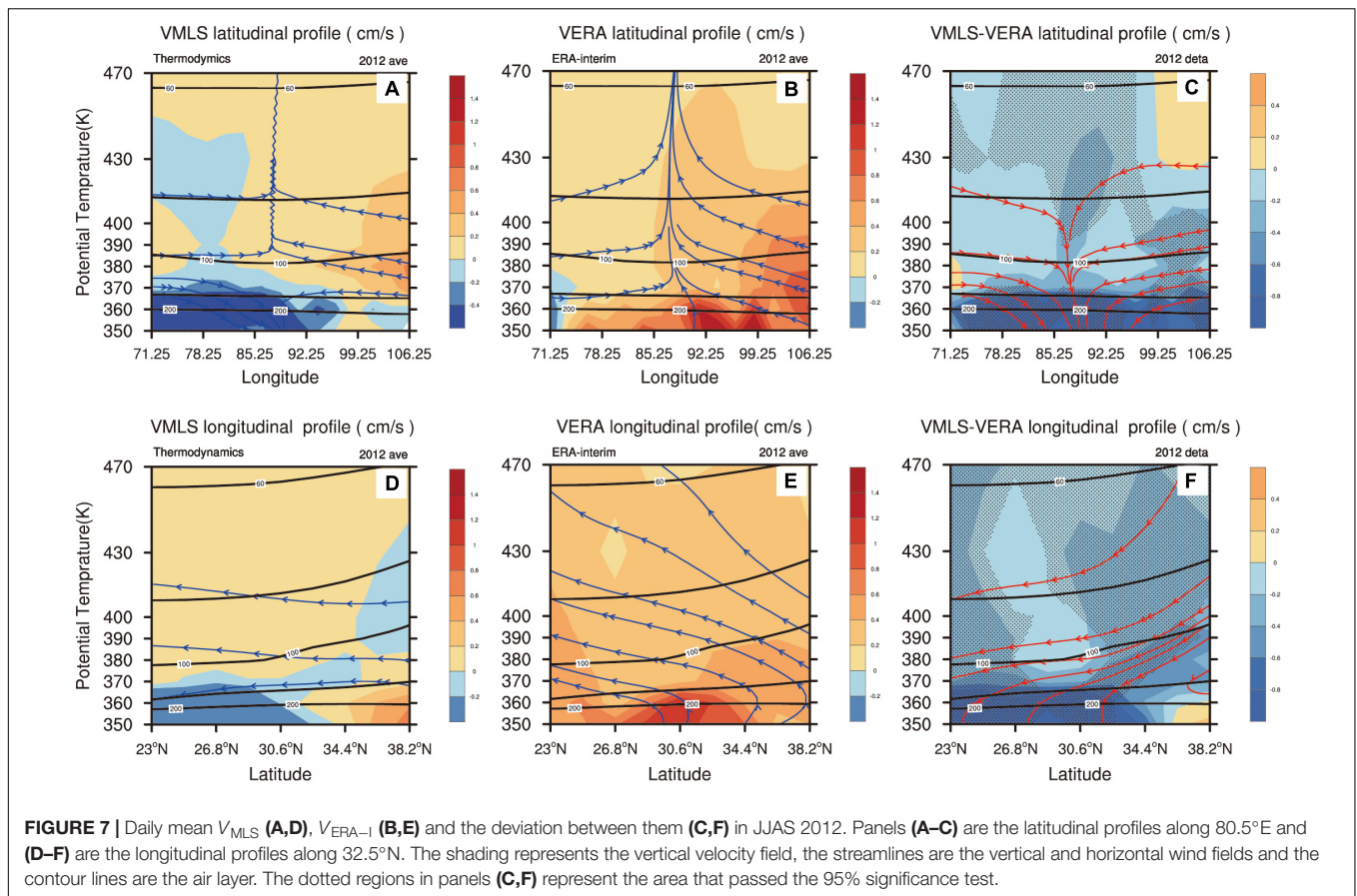
FIGURE 4 | Average deviation (solid lines) and standard error (dashed lines) between V_{AIRS} and V_{ERA-I} for 2012 **(A,B)** and 2016 **(C,D)**. The upper panels are daytime and the bottom panels nighttime.

FIGURE 5 | Daily mean V_{MLS} **(A,D)**, V_{ERA-I} **(B,E)** and the deviation between them **(C,F)** for daytime in JJAS 2012. Panels **(A–C)** are the latitudinal profiles along 80.5°E and **(D–F)** are the longitudinal profiles along 32.5°N. The shading represents the vertical velocity field, the streamlines are the vertical and horizontal wind fields and the contour lines are the air layer. The dotted regions in panels **(C,F)** represent the area that passed the 95% significance test.

FIGURE 6 | Daily mean V_{MLS} **(A,D)**, V_{ERA-I} **(B,E)** and the deviation between them **(C,F)** for the nighttime in JJAS 2012. Panels **(A–C)** are the latitudinal profiles along 80.5°E and **(D–F)** are the longitudinal profiles along 32.5°N. The shading represents the vertical velocity field, the streamlines are the vertical and horizontal wind fields and the contour lines are the air layer. The dotted regions in panels **(C,F)** represent the area that passed the 95% significance test.

FIGURE 7 | Daily mean V_{MLS} **(A,D)**, V_{ERA-I} **(B,E)** and the deviation between them **(C,F)** in JJAS 2012. Panels **(A–C)** are the latitudinal profiles along 80.5°E and **(D–F)** are the longitudinal profiles along 32.5°N. The shading represents the vertical velocity field, the streamlines are the vertical and horizontal wind fields and the contour lines are the air layer. The dotted regions in panels **(C,F)** represent the area that passed the 95% significance test.

existing here, a downdraft occurs in this region. We suggest that V_{MLS} can describe the descending motion more clearly. The ascending movement of V_{MLS} is significantly weaker than V_{ERA-I} in the same region.

Figure 6 shows that V_{MLS} is mainly subsiding in the northwest and reaches the upper troposphere, whereas V_{ERA-I} is mainly subsiding in the lower layers in the west with a stronger intensity center. The descending motion of V_{MLS} below 150 hPa shows that there is a vertical divergence at 150 hPa in the west and north of the ASMA region. This result is consistent with that of V_{Ali} and V_{AIRS} at night.

Figure 7 shows the overall daily mean vertical velocity of JJAS in 2012. The distributions of both V_{MLS} and V_{ERA-I} are more consistent with the characteristics in daytime (**Figure 5**), indicating that the vertical motion in the ASMA region depends mainly on the vertical velocity in the daytime. The ascending movement of V_{MLS} is weaker than that of V_{ERA-I}, but still reflects the subsiding circulation in the western and northern ASMA.

DISCUSSION AND CONCLUSION

Conclusion

The thermodynamic method has theoretical advantages over the kinematic method for calculating the vertical velocity over the ASMA region. We established a method based on the

thermodynamic equation and introduced heating rate data obtained from *in situ* observations and revised satellite data from MLS/AIRS to determine the vertical velocity in JJAS 2012 and 2106. By comparing V_{AIRS}, V_{Ali}, and V_{MLS} with V_{ERA-I}, we found that V_{Ali} and V_{ERA-I} present similar behavior in upper troposphere, with a reversal of the wind direction near 150 and 80 hPa during the night in JJAS 2012. A comparison of V_{AIRS} and V_{ERA-I} showed that V_{AIRS} behaved differently from V_{ERA-I} at daytime. V_{AIRS} ascended weakly below 150 hPa and reversed to descending then reaches zero at 100 hPa, while V_{ERA-I} was clearly shown ascending in all layers. At nighttime, V_{AIRS} has similar behaviors of V_{ERA-I} with a weaker vertical motion intensity, which are also consistent with V_{Ali}. The differences between them have statistical significance with the degree of credibility in one standard error. We consider that V_{AIRS} is more in line with V_{ERA-I} in 2012 and better describes the vertical motion in the ASMA region.

The vertical profiles both day and night of V_{MLS} along (32.5°N, 80.5°E) illustrated that upward motions are in the east and south, and descending motions are in the west and north over the ASMA region, while V_{ERA-I} only showed descending motions in the west and north at the nighttime. The local flow of the Hadley Circulation and the Brewer-Dobson Circulation in this region may show a downdraft directly in the north. Besides, as a result of the weaker heating of the Iranian Plateau in the west than the Qinghai–Tibet Plateau in the east, the ascending motion

over the Iranian Plateau is weaker than that over the Qinghai–Tibet Plateau (Zhang F. et al., 2017). Therefore, the vertical motions over the Iranian Plateau mainly present descending. We suggest that V_{MLS} can describe the vertical motions over the ASMA more accurately—that is, descending in the west and north and ascending in the east and south. The two vertical velocity profiles were similar in the ASMA region during the night-time. Based on the daily mean vertical velocity, we found that the vertical motion over the ASMA region mainly depends on the vertical velocity in the daytime.

Discussion

The thermodynamic vertical velocity we calculated is slightly weaker than the reanalysis data in some areas over the ASMA, which is inconsistent with the expectation that the velocity obtained by the kinematics method is insufficient. The probable reasons for this deviation are as follows. (1) The radiative heating rate used in this paper resulted in an inaccurate diabatic calculation. (2) For consistency, the variables u, v, T, and $\dot{Q}$ were interpolated vertically to fixed isentropic (θ) levels. However, a variable in adjacent grids has different staggered changes in the vertical direction. After interpolation, the original vertical distribution characteristics would be eliminated, thereby introducing a deviation (Rex et al., 2008). (3) The deviations in the ERA-I dataset cannot be neglected and new reanalysis data should be analyzed in the future (Gao et al., 2014; Gianpaolo et al., 2015).

REFERENCES

Antokhin, P. N., and Belan, B. D. (2013). Control of the dynamics of tropospheric ozone through the stratosphere. *J. Atmos. Ocean. Opt.* 26, 207–213. doi: 10.1134/S1024856013030032

Aschmann, J., Sinnhuber, B.-M., and Atlas, E. L. (2009). Modeling the transport of very short-livedsubstances into the tropical upper troposphere and lower stratosphere. *Atmosp. Chem. Phys.* 3, 9237–9247.

Bergman, J. W., Fierli, F., Jensen, E. J., Honomichl, S., and Pan, L. L. (2013). Boundary layer sources for Asian anticyclone: regional contributions to a vertical conduit. *J. Geophys. Res.* 118, 2560–2575. doi: 10.1002/jgrd.50142

Bergman, J. W., Jensen, E. J., and Pfister, L. (2012). Seasonal differences of vertical-transport efficiency in the tropical tropopause layer: on the interplay between tropical deep cobvection, large-scale vertical ascent, and horizontal circulations. *J. Geophys. Res.* 117:D05302. doi: 10.1029/2011JD016992

Bian, J. C. (2009). Recent advances in the study of atmospheric vertical structures in upper troposphere and lower stratosphere. *Adv. Earth Sci.* 16(Suppl. 1), 116–122.

Bian, J. C., Fan, Q. J., and Yan, R. C. (2013). Summertime stratosphere-tropospherestratosphere–troposphere exchange over the tibetan plateau and its climatic impact. *Adv. Meteor. Sci. Technol.* 2, 22–28.

Bian, J. C., Li, D., Bai, Z. X., Li, Q., Lyu, D., and Zhou, X. (2020). Transport of Asian surface pollutants to the global stratosphere from the Tibetan Plateau region during the Asian summer monsoon. *Natl. Sci. Rev.* 5:nwaa005.

Bian, J. C., Yan, R. C., and Chen, H. B. (2011a). Tropospheric pollutant transport to the stratosphere by Asian summer monsoon. *Chin. J. Atmos. Sci.* 35, 897–902.

Bian, J. C., Yan, R. C., Chen, H. B., Lu, D., and Massie, S. T. (2011b). Formation of the summertime ozone valley over the Tibetan Plateau: the Asian summer monsoon and air column variations. *Adv. Atmos. Sci.* 28, 1318– 1325.

Butchart, N., and Scaife, A. A. (2001). Removal of chlorofluorocarbons by increased mass exchange between stratosphere and troposphere in a changing climate [climate [J]. *Nature* 2001, 799–802.

Chen, B., Xu, X. D., and Bian, J. C. (2010). Sources, path ways and time scales for the troposphere to stratosphere transport over Asian m on snoon regions in boreal summer. *J. Chinese J. Atmos. Sci.* 34, 495–505.

Chen, D., Zhou, T. J., Ma, L. Y., Shi, C. H., Guo, D., and Chen, L. (2019). Statistical analysis of the spatiotemporal distribution of ozone induced by cut-off lows in the upper troposphere and lower stratosphere over northeast Asia. *Atmosphere* 10:696. doi: 10.3390/atmos10110696

Chipperfield, M. P. (2006). New version of the TOMCAT/SLIMCAT offline chemical transport model: intercomparison of stratospheric tracer experiments. *Q. J. R. Meteorol. Soc.* 132, 1179–1203. doi: 10.1256/qj.05.51

Cong, C. H., Li, W. L., and Zhou, X. J. (2001). Mass exchange between stratosphere and troposphere over the qinghai-tibet Qinghai–Tibet plateau and its vicinity. *J. Chinese Sci. Bull.* 46, 1914–1918.

Considine, D. B., Logan, J. A., and Olsen, M. A. (2008). Evaluation of near-tropopause ozone distributions in the global modeling initiative combined stratosphere/troposphere model with ozonesonde data. *Atmos. Chem. Phys.* 8, 2365–2385.

Davis, J., Collier, C., Davies, F., and Burton, R. (2007). Vertical velocity observed by Doppler lidar during cops – A case study with a convective rain event. *Meteorol. Z.* 22, 463–470.

Deng, F., Jones, D. B. A., and Walker, T. W. (2015). Sensitivity analysis of the potential impact of discrepancies in stratosphere-tropospherestratosphere–troposphere exchange on inferred sources and sinks of CO2. *Atmos. Chem. Phys.* 15, 10813–10851.

Dessler, A. E., and Sherwood, S. C. (2004). Effect of convection on the summertime extratropical lower stratosphere. *J. Geophys. Res.* 109:D23301.

Dobbie, J. S., Li, J., and Chýlek, P. (1999). Two- and four-stream optical properties for water clouds and solar wavelengths. *J. Geophys. Res. Atmos.* 104, 2067–2080. doi: 10.1029/1998JD200039

Elliot, S., and Rowland, F. S. (1987). Chlorofluorocarbons and stratospheric ozone [ozone. *J. Chem. Educ.* 64, 387–380.

Eluszkiewicz, J., David, C., Richard, Z., Lee, E., Evan, F., Lucien, F., et al. (1996). Residual circulation in the stratosphere and lower mesosphere as diagnosed from Microwave Limb Sounder data. *J. Atmos. Sci.* 53, 217–240. doi: 10.1175/1520-04691996053<0217:RCITSA$>$2.0.CO;2

Eluszkiewicz, J., Hemler, R. S., Mahlman, J. D., Bruhwiler, L., and Takacs, L. L. (2000). Sensitivity of age-of-air calculations to the choice of advection scheme. *J. Atmos. Sci.* 57, 3185–3201.

Fan, Q. J., Bian, J. C., and Pan, L. L. (2017a). Atmospheric boundary layer sources for upper tropospheric air over the Asian summer monsoon region. *Atmos. Oceanic Sci. Lett.* 10, 358–363.

Fan, Q. J., Bian, J. C., and Pan, L. L. (2017b). Stratospheric entry point for upper-tropospheric air within the Asian summer monsoon anticyclone. *Sci. China Earth Sci.* 60, 1685–1693.

Fan, W. X., Wang, W. G., and Bian, J. C. (2008). The distribution of cross-tropopause mass flux over the Tibetan Plateau and its surrounding regions. *Chin. J. Atmos. Sci.* 32, 1309–1318.

Fu, R., Hu, Y. L., Wright, J. S., Jiang, J. H., Dickinson, R. E., Chen, M., et al. (2006). Short circuit of water vapor and polluted air to the global stratosphere by convective transport over the Tibetan Plateau. *Proc. Natl. Acad. Sci. U.S.A.* 103, 5664–5669.

Fueglistaler, S., Bonazzola, M., Haynes, P. H., and Peter, T. (2005). Stratospheric water vapor predicted from the Lagrangian temperature history of air entering the stratosphere in the tropics. *J. Geophys. Res. Atmos.* 110. doi: 10.1029/2004JD005516

Gamelin, B., and Carvalho, L. (2017). *Tropopause Ozone and Water Vapor Concentrations During the South American Monsoon System With AIRS Satellite Observations and MERRA-2 Data.* Washington, DC: American Geophysical Union.

Gao, L., Hao, L., and Chen, X. W. (2014). Evaluation of ERA-interim monthly temperature data over the Tibetan Plateau. *J. Mountain Sci.* 11, 1154– 1168.

Gerber, E. P. (2015). The stratosphere and its coupling to the troposphere and beyond. *J. Encycl. Appl. Comput. Mat.* 2015:1676. doi: 10.1007/978-3-540-70529-1_573

Gettelman, A., Kinnison, D. E., and Dunkerton, T. J. (2004). Impact of monsoon circulations on the upper troposphere and lower stratosphere. *J. Geophys. Res.* 109:D22101.

Gianpaolo, B., Albergel, C., and Beljaars, A. (2015). ERA-Interim/Land: a global land surface reanalysis dataset. *Hydrol. Earth Syst. Sci.* 19, 389–407.

Guo, D., Su, Y. C., Shi, C. H., and Xu, J. (2015). Double core of ozone valley over the Tibetan Plateau and its possible mechanisms. *J. Atmos. Solar Terres. Phys.* 13, 127–131.

Guo, D., Su, Y. C., and Zhou, X. (2017). Evaluation of the trend uncertainty in summer ozone valley over the Tibetan Plateau in three reanalysis datasets. *J. Meteorol. Res.* 31, 431–437.

Guo, D., Wang, P., Zhou, X., Liu, Y., and Li, W. (2012). Dynamic effects of the South Asian high on the ozone valley over the Tibetan Plateau. *Acta Meteorol. Sin.* 26, 216–228.

He, Y., Sheng, Z., and He, M. (2020a). Spectral analysis of gravity waves from near space high-resolution balloon data in Northwest China. *Atmosphere* 11:133. doi: 10.3390/atmos11020133

He, Y., Sheng, Z., and He, M. (2020b). The first observation of turbulence in northwestern china by a near-space high-resolution balloon sensor. *Sensors* 20:677. doi: 10.3390/s20030677

Herman, R., Rosenlof, K. H., Ray, E. A., Bedka, K. M., Read, W. G., Chin, K., et al. (2017). Enhanced stratospheric water vapor over the summertime continental United States and the role of overshooting convection. *Atmos. Chem. Phys.* 17, 6113–6124.

Holton, J. R. (1990). On the global exchange of mass between the stratosphere and troposphere. *J. Atmos. Sci.* 47, 331–344.

Holton, J. R., Haynes, P. H., and McIntyre, M. E. (1995). Stratosphere troposphere exchange. *Rev. Geophys.* 33, 403–439.

Hu, Y. Y., Ding, F., and Xia, Y. (2009). Long-term trend of stratospheric atmosphere under global changing conditions. *J. Adv. Earth Sci.* 024, 242–251.

Huang, R., Wen, C., and Ke, W. (2018). Atmospheric dynamics in the stratosphere and its interaction with tropospheric processes: progress and problems. *Chinese J. Atmos. Sci.* 42, 463–487. doi: 10.3878/j.issn.1006-9895.1802.17250

King, M. D., Menzel, W. P., Kaufman, Y. J., Tanre, D., Gao, B.-C., Platnick, S., et al. (2003). Cloud and aerosol properties, precipitable water, and profiles of temperature and humidity from MODIS. *IEEE Trans. Geosci. Remote Sens.* 41, 442–458. doi: 10.1109/TGRS.2002.808226

Kishcha, P., Starobinets, B., and Alpert, P. (2007). Latitudinal variations of cloud and aerosol optical thickness trends based on MODIS satellite data. *Geophys. Res. Lett.* 34:L05810. doi: 10.1029/2006GL028796

Kistler, R. E., Kalnay, E., Collins, W., and Saha, S. (2001). The NCEP-NCAR 50-year reanalysis: monthly means CD-ROM and documentation. *Bull. Am. Meteorol. Soc.* 82, 247–268.

Krishnamurti, T. N., and Bounoua, L. (1996). *An Introduction to Numerical Weather Prediction Techniques.* Boca Raton, FL: CRC Press.

Kuang, S., Newchurch, M. J., Burris, J., Wang, L., Knupp, K., and Huang, G. (2012). Stratosphere-to-troposphere transport revealed by ground-based lidar and ozonesonde at a midlatitude site. *J. Geophys. Res. Atmos.* 117:305. doi: 10.1029/2012JD017695

Li, C. M., Hu, J. X., and Xu, J. H. (2005). Prediction on the influence of ozone depletion substance to the stratospheric ozone. *China Environ. Sci.* 25, 142–145.

Li, J. N., and Barker, H. (2005). A radiation algorithm with correlated-k distribution. *J. Atmos. Sci.* 62, 286–309. doi: 10.1175/JAS-3396.1

Li, J. N., Ma, X., Salzen K.V., and Dobbie, S. (2008). Parameterization of sea salt optical properties anda related radiative forcing study. *Atmos. Chem. Phys.* 8, 4787–4798. doi: 10.5194/acp-8-4787-2008

Li, Z. K., Qin, H., and Guo, D. (2017). Impact of ozone valley over the Tibetan Plateau on the South Asian high in CAM5. *Adv. Meteorol.* 2017:9383495.doi: 10.1155/2017/9383495

Lindner, T. H., and Li, J. (2000). Parameterization of the optical properties for water clouds in the infrared. *J. Climate* 13, 1797–1805. doi: 10.1175/1520-0442(2000)013<1797:POTOPF>2.0.CO;2

Liu, Y. (1998). Atmospheric ozone layer, ultraviolet radiation and human health. *Adv. Geophys.* 13, 103–110.

Liu, Y. (2007). Trends of stratospheric ozone and aerosols over tibetan plateau. *J. Acta* 65, 938–945.

Liu, Y., Li, W., and Zhou, X. (2003). Mechanism of formation of the ozone valley over the Tibetan Plateau in summer— transport and chemical process of ozone. *Adv. Atmos. Sci.* 20, 103–109.

London, J., and Park, J. H. (2011). The interaction of ozone photochemistry and dynamics in the stratosphere. *Three Dimens. Atmos. Model.* 52, 1599– 1609.

Lord, S. J., and Jacqueline, M. L. (1988). Vertical velocity structures in an axisymmetric, nonhydrostatic tropical cyclone model. *J. Atmos. Sci.* 45, 1453– 1461.

Lu, C. H., and Ding, Y. H. (2013). Advances in the study of stratospheric and tropospheric interactions. *J. Prog. Meteorol. Technol.* 2013, 6–21. doi: 10.3969/j.issn.2095-1973.2013.02.001

Lv, D. R., Bian, J. C., and Chen, B. H. (2009). The frontier and importance of the study of stratospheric atmospheric processes. *Adv. Earth Sci.* 24, 221–228.

Mahowald, N. M., Plumb, R. A., and Rasch, P. J. (2002). Stratospheric transport in a three-dimensional isentropic coordinate model. *J. Geophys. Res. Atmos.* 107, ACH3-1–ACH3-14.

Monge-Sanz, B. M., Chipperfield, M. P., Simmons, A. J., and Uppala, S. M. (2007). Mean age of air and transport in a CTM: comparison of different ECMWF analyses. *Geophys. Res. Lett.* 34:L04801.

Newman, P. (2014). "The Future of the Stratosphere and the Ozone Layer[C]," in *Proceedings of the Agu Fall Meeting*, (Washington, DC: AGU).

Newman, P. A., Oman, L. D., and Douglass, A. R. (2009). What would have happened to the ozone layer if chlorofluorocarbons (CFCs) had not been regulated? *Atmos. Chem. Phys.* 9, 2113–2128.

Oram, D. E., Ashfold, M. J., Laube, J. C., Gooch, L. J., Humphrey, S., Sturges, W. T., et al. (2017). A growing threat to the ozone layer from short-lived anthropogenic chlorocarbons. *Atmos. Chem. Phys. Discuss.* 2017, 1–20.

Park, M., Randel, W. J., Gettelman, A., Massie, S. T., and Jiang, J. H. (2007). Transport above the Asian summer monsoon anticyclone inferred from Aura Microwave Limb Sounder tracers. *J. Geophys. Res. Atmos.* 112:309. doi: 10.1029/2006JD008294

Pavlov, A. N., Stolyarchuk, S. Y., Shmirko, K. A., and Bukin, O. A. (2013). Lidar measurements of variability of the vertical ozone distribution caused by the stratosphere-troposphere exchange in the Far East Region. *J. Atmos. Ocean. Opt.* 26, 126–134. doi: 10.1134/S10248560130 20115

Ploeger, F., Konopka, P., Gunther, G., Groob, J. U., and Muller, R. (2010). Impact of the vertical velocity scheme on modeling transport in the tropical tropopause layer. *J. Geophys. Res. Atmos.* 115:301. doi: 10.1029/2009JD012023

Platnick, S., King, M. D., Ackerman, S. A., Menzel, W. P., Baum, B. A., Riedi, J. C., et al. (2003). The modis cloud products: algorithms and examples from terra. *IEEE Trans. Geosci. Remote Sens.* 41, 459–473. doi: 10.1109/TGRS.2002.808301

Randel, W. J., Garcia, R. R., and Wu, F. (2002). Time-dependent upwelling in the tropical lower stratosphere estimated from the zonal-mean momentum budget. *J. Atmos. Sci.* 59, 2141–2152.

Randel, W. J., and Jensen, E. (2013). Physical processes in the tropical tropopause layer and their role in a changing climate. *Nat. Geosci.* 6, 169–176.

Randel, W. J., Park, M., and Emmons, L. (2010). Asian monsoon transport of pollution to the stratosphere. *Science* 328, 611–613.

Rex, M., Lehmann, R., and Wohltmann, I. (2008). Ascent rates, dehydration and vertical diffusion in the tropical tropopause region and lower stratosphere. *Reunion Island Symposium* 37:2605.

Rodgers, C. D. (1990). Characterization and error analysis of profiles retrieved from remote sonde measurements. *Geophys. Res.* 95, 5587–5595.

Rosenlof, K. (1995). Seasonal cycle of the residual mean meridional circulation in the stratosphere. *J. Geophys .Res. Atmos.* 100:5173. doi: 10.1029/94jd03122

de Roode, S. R., Siebesma, A. P., Jonker, H. J. J., and de Voogd, Y. D. (2012). Parameterization of the vertical velocity equation for shallow cumulus clouds. *J. Mon. Weather Rev.* 140:2424. doi: 10.1175/MWR-D-11-00277.1

Salzen, K. V., Scinocca, J. F., Mcfarlane, N. A., Li, J., Cole, J. N. S., Plummer, D., et al. (2013). The canadian fourth generation atmospheric global climate model (canam4). Part I: representation of physical processes. *Atmos. Ocean* 51, 104–125. doi: 10.1080/07055900.2012.755610

Schauffler, S. M., Atlas, E. L., Blake, D. R., Flocke, F., Lueb, R. A., Lee-Taylor, J. M., et al. (1999). Distributions of brominated organic compounds in the troposphere and lower stratosphere. *J. Geophys. Res.* 104: 21513.

Schoeberl, M. R., Douglass, A. R., Zhu, Z., and Pawson, S. (2003). Comparison of the lower stratospheric age spectra derived from a general circulation model and two data assimilation systems. *J. Geophys. Res.* 108:4113.

Shepherd, T. (2002). Issues in stratosphere-tropospherestratosphere–troposphere coupling. *J. Meteorol. Soc. Jpn.* 80, 769–792.

Sherman, L. (1953). Estimates of the vertical velocity based on the vorticity equation. *J. Atmos. Sci.* 10, 399–400.

Shi, C. H., Huang, Y., and Guo, D. (2018). Comparison of trends and abrupt change of Asia High from 1979 to 2010 in Reanalysis and Radiosonde data. *J. Atmos. Solar Terrest. Phys.* 170, 48–54. doi: 10.1016/j.jastp.2018.02.005

Shi, C. H., Zhang, C. X., and Guo, D. (2017). Comparison of electrochemical concentration cell ozonesonde and microwave limb sounder satellite remote sensing ozone profile for the center of the South Asian High. *Remote Sens.* 9:1012.

Sofieva, V. F., Ialongo, I., Hakkarainen, J., Kyölä, E., Tamminen, J., Laine, M., et al. (2017). Improved GOMOS/Envisat ozone retrievals in the upper troposphere and the lower stratosphere. *J. Atmos. Meas. Tech.* 10, 231–246. doi: 10.5194/amt-10-231-2017

Stohl, A., Bonasoni, P., Cristofanelli, P., Collins, W., Feichter, J., Frank, A., et al. (2003). Stratosphere-roposphere exchange: a review, and what we have learned from STACCATO. *J. Geophys. Res. Atmos.* 108, 469–474.

Tang, Z., Guo, D., and Su, Y. C. (2019). Double cores of the Ozone Low in the vertical direction over the Asian continent in satellite data sets. *Earth Planet. Phys.* 3, 11–19.

Tian, H. Y., Tian, W. S., Luo, J., Zhang, J., and Zhang, M. (2017). Climatology of cross-tropopause mass exchange over the Tibetan Plateau and its surroundings. *Int. J. Climatol.* 37, 3999–4014.

Tian, W. S., Martyn, C., and Huang, Q. (2008). Effects of the Tibetan Plateau on total column ozone distribution. *Tellus B* 60, 622–635.

Tian, W. S., Zhang, M., and Shu, J. C. (2009). Application and development prospect of middle atmosphere model. *J. Adv. Earth Sci.* 024, 252–261.

Uma, K. N., and Rao, T. N. (2009). Characteristics of vertical velocity cores in different convective systems observed over Gadanki, India. *Am. Meterol. Soc.* 2009, 954–975.

Vaughan, G., Price, J. D., and Howells, A. (1994). Transport into the troposphere in a tropopause fold. *Q. J. R. Meteorol. Soc.* 120, 1085–1103.

Vernier, J. P., Pommereau, J. P., Garnier, A., Pelon, J., Larsen, N., Nielsen, J., et al. (2009). Tropical stratospheric aerosol layer from CALIPSO lidar observations. *J. Geophys. Res. Atmos.* 114:D00H10. doi: 10.1029/2009JD011946

Von Clarmann, T. (2006). Validation of remotely sensed profiles of atmospheric state variables: strategies and terminology. *Atmos. Chem. Phys.* 6, 4311–4320.

Wang, H., Wang, W., Ding, A., and Huang, X. (2019). Impacts of stratosphere-troposphere-transport on summertime surface ozone over Eastern China. *J. Sci. Bull.* 65, 253–334. doi: 10.1016/j.scib.2019.11.017

Wang, Y., Wang, H., and Wang, W. A. (2020). Stratospheric intrusion-influenced ozone pollution episode associated with an intense horizontal-trough event. *Atmosphere* 11:164.

Xie, F., Li, J., Tian, W., Feng, J., and Huo, Y. (2012). The Signals of El Niño Modoki in the tropical tropopause layer and stratosphere. *Atmos. Chem. Phys.* 12, 5259–5273.

Xie, F., Li, J., Tian, W., Fu, Q., Jin, F.-F., Hu, Y., et al. (2016). A connection from Arctic stratospheric ozone to El Niño-Southern oscillation. *Environ. Res. Lett.* 11:124026.

Yan, X., Zheng, X., Zhou, X., Vomel, H., Song, J. Y., Li, W., et al. (2015). Validation of Aura Microwave Limb Sounder water vapor and ozone profiles over the Tibetan Plateau and its adjacent region during boreal summer. *Sci. China Earth Sci.* 58, 589–603.

Yan, X. L., Konopka, P., and Ploeger, F. (2019). The efficiency of transport into the stratosphere via the Asian and North American summer monsoon circulations. *Atmos. Chem. Phys.* 19, 15629–15649.

Yang, J., Shen, Z., and Lu, D. (2004). Simulation of stratosphere–troposphere exchange effecting on the distribution of ozone over eastern Asia. *Chin. J. Atmos. Sci.* 28, 579–588.

Yu, P., Rosenlof, K. H., and Liu, S. (2017). Efficient transport of tropospheric aerosol into the stratosphere via the Asian summer monsoon anticyclone. *Proc. Natl. Acad. Sci. U.S.A.* 2017, 6972–6977.

Yu, Z. X., Guo, D., and Li, L. P. (2020). The characteristics and mechanism of Rossby-wave energy vertical propagation crosssing tropopause in South Asia High region. *Chinese Grophys.* 63, 73–85. doi: 10.6038/cjg2020L 0626

Zhan, R. F., and Li, J. P. (2012). Relationship of interannual variations of the stratosphere –troposphere exchange of water vapor with the Asian summer monsoon. *Chinese J. Geophys.* 55, 3181–3193. doi: 10.6038/j.issn.0001-5733. 2012.10.001

Zhang, F., Kun, W., and Li, J. N. (2018). Radiative transfer in the region with solar and infrared spectra overlap. *J. Quant. Spectrosc. Radiat. Trans.* 219, 366–378.

Zhang, F., and Li, J. (2013). Doubling-adding method for delta-four-stream spherical harmonic expansion approximation in radiative transfer parameterization. *J. Atmos. Sci.* 70, 3084–3101.

Zhang, F., Shen, Z., and Li, J. (2013). Analytical delta-four-stream doubling-adding method for radiative transfer parameterizations. *J. Atmos. Sci.* 70, 794–808.

Zhang, F., Wu, K., Li, J., Yang, Q., Zhao, J.-Q., and Li, J. (2016). Analytical infrared delta-four-stream adding method from invariance principle. *J. Atmos. Sci.* 73, 4171–4188.

Zhang, F., Wu, K., Liu, P., Jing, X. W., and Li, J. (2017). Accounting for Gaussian quadrature in four-stream radiative transfer algorithms. *J. Quant. Spectrosc. Radiat. Trans.* 192, 1–13.

Zhang, H. X., Li, W. J., and Li, W. P. (2017). Spatial and temporal distribution characteristics of surface heat fluxes over both Tibetan Plateau and Iranian Plateau in boreal spring and summer and their relationships. *J. Acta Meteorol. Sin.* 75, 260–274.

Zhang, H., Jing, X., and Li, J. (2014). Application and evaluation of a new radiation code under McICA scheme in BCC_AGCM2.0.1. *Geosci. Model Dev.* 7, 737–754.

Zhang, H., Wang, Z., and Zhang, F. (2015). Impact of four-stream radiative transfer algorithm on aerosol direct radiative effect and forcing. *Int. J. Climatol.* 35, 4318–4328.

Zhang, J., Tian, W., and Chipperfield, M. P. (2015). Persistent shift of the Arctic polar vortex towards the Eurasian continent in recent decades. *Nat. Clim. Change* 6:1094.

Zhang, J., Tian, W., Xie, F., Chipperfield, M. P., Feng, W., Son, S.-W., et al. (2018). Stratospheric ozone loss over the Eurasian

continent induced by the polar vortex shift. *Nat. Commun.* 9: 206.

Zhang, J., Tian, W., Xie, F., Tian, H., Luo, J., Zhang, J., et al. (2014). Climate warming and decreasing total column ozone over the Tibetan Plateau during winter and spring. *Tellus B* 66:23415.

Zheng, X. D., Tang, J., and Li, W. L. (1998). Observational study on total ozone amount and its vertical profile over Lhasa in the summer of 1998. *J. Appl. Meteor. Sci.* 11, 173–179.

Zhou, X. G., Wang, X. M., and Tao, Z. Y. (2014). Review and Discussion of Isentropic Thinking and Isentropic Potential Vorticity Thinking. *Meteorological* 40, 521–529.

Zhou, X. J., and Luo, C. (1994). Ozone valley over Tibetan plateau. *J. Meteor. Res.* 8, 505–506.

Zhou, X. J., Luo, C., and Li, W. L. (1995a). The change of total ozone in China and the low value center of qinghai-tibet Qinghai–Tibet plateau. *J. Chinese Sci. Bull.* 40:1396.

Zhou, X. J., Luo, C., and Li, W. L. (1995b). The column ozone variation in China and the low value ozone center over Tibetan Plateau. *Chin. Sci. Bull.* 40, 1396–1398.

Zou, H., and Gao, Y. Q. (1997). Vertical ozone profile over Tibet using SAGE I and II data. *Adv. Atmos. Sci.* 14, 505–512.

APPENDIX A

Beijing Climate Center Radiation Transfer Model

A radiation model in Canadian Atmospheric Global Climate Model called CanAM4.3_RAD (Salzen et al., 2013) is used in this study. In this model, the correlated-k distribution (CKD) method of Li and Barker (2005) is used for gaseous transmission, including most of the greenhouse gases H_2O, O_3, CH_4, CO_2, N_2O, CO, O_2, CFC and so on. To improve the accuracy of the calculation in the ASMA region, the H_2O and O_3 were introduced from the in situ observations at Ali station and the revised satellite sounding data of the MLS and AIRS (Shi et al., 2017). The cloud properties (e.g., cloud top pressure, cloud effective radius, cloud water path, cloud fraction) were provided by Level 3 Moderate Resolution Imaging Spectroradiometer (MODIS) gridded global monthly products (MOD08_M3) data (King et al., 2003; Platnick et al., 2003; Kishcha et al., 2007). The other gases components were constant set in model. Four solar bands are adopted in wavenumber ranges 14500–50000, 8400–14500, 4200–8400, 2500–4200 cm^{-1} and nine infrared bands are adopted in wavenumber ranges 2200–2500, 1900–2200, 1400–1900, 1100–1400, 980–1100, 800–980, 540–800, 340–540, 0–340 cm^{-1}. Optical properties of aerosols and cloud particles vary relatively slowly with wavenumber so they are parameterized as appropriately weighted mean values over each of the wavenumber intervals with aerosols and cloud optical properties respectively (Dobbie et al., 1999; Lindner and Li, 2000; Li et al., 2008). To achieve the high accuracy of heating/cooling rates, we use the adding method of four-stream spherical harmonic expansion approximation (4SDA) for solar radiation (Zhang and Li, 2013) and the adding method of four-stream discrete ordinates (4DDA) for infrared radiation (Zhang et al., 2016; Zhang J. et al., 2018; Zhang H.X. et al., 2017).